Local Characteristic Decomposition Based Central-Upwind Scheme for Compressible Multifluids

Shaoshuai Chu and Alexander Kurganov

Abstract In this paper, we introduce the local characteristic decomposition based central-upwind (LCD-CU) scheme for compressible multifluids. The scheme is implemented within the hybrid multifluid algorithm from [A. CHERTOCK, S. CHU, AND A. KURGANOV, J. Sci. Comput, 89(2021), Paper No. 48], according to which we use the level set method to track the position of material interfaces and replace the conservative compressible Euler equations with the pressure-based nonconservative ones in the vicinities of the interfaces. The LCD-CU scheme is used away from the interfaces and this helps to reduce the numerical dissipation in these areas. At the interfaces, we still use the path-conservative central-upwind scheme designed to accurately solve nonconservative hyperbolic systems. This leads to a substantially higher resolution, especially in the two-dimensional case.

Keywords Path-conservative scheme · Compressible multifluids · Local characteristic decomposition based central-upwind scheme · Hybrid algorithm

1 Introduction

This paper focuses on the development of a new numerical method for compressible multifluids, which are assumed to be immiscible. The governing equations in the two-dimensional (2-D) case read as

S. Chu
Department of Mathematics, Southern University of Science and Technology, Shenzhen 518055, China
e-mail: chuss2019@mail.sustech.edu.cn

A. Kurganov (✉)
Department of Mathematics, Shenzhen International Center for Mathematics, and Guangdong Provincial Key Laboratory of Computational Science and Material Design, Southern University of Science and Technology, Shenzhen 518055, China
e-mail: alexander@sustech.edu.cn

E. Franck et al. (eds.), *Finite Volumes for Complex Applications X—Volume 2, Hyperbolic and Related Problems*, Springer Proceedings in Mathematics & Statistics 433,
https://doi.org/10.1007/978-3-031-40860-1_8

$$\rho_t + (\rho u)_x + (\rho v)_y = 0, \tag{1}$$
$$(\rho u)_t + (\rho u^2 + p)_x + (\rho uv)_y = 0, \tag{2}$$
$$(\rho v)_t + (\rho uv)_x + (\rho v^2 + p)_y = 0, \tag{3}$$
$$E_t + [u(E+p)]_x + [v(E+p)]_y = 0, \tag{4}$$

where x and y are spatial variables, t is time, and $\rho(x, y, t)$, $u(x, y, t)$, $v(x, y, t)$, $p(x, y, t)$, and $E(x, y, t)$ are the density, x- and y-velocities, pressure, and total energy, respectively.The system is completed through the following equations of state (EOS) for each of the fluid components:

$$p = (\gamma - 1)\Big[E - \frac{\rho}{2}(u^2 + v^2)\Big] - \gamma p_\infty, \tag{5}$$

where γ represents the specific heat ratio and p_∞ is the stiffness parameter, with $p_\infty = 0$ corresponding to the ideal gas case. In this paper, we consider a multifluid problem with two components and assume that $\gamma = \gamma_I$, $p_\infty = p_{\infty,I}$ and $\gamma = \gamma_{II}$, $p_\infty = p_{\infty,II}$ for the first and second fluid components, respectively.

The fluid components can be identified, for instance, by the level-set function ϕ whose zero level-set defines the interface between the fluid components; see [1, 3, 10, 16]. The function ϕ propagates with the fluid velocity and satisfies the following conservative equation:

$$(\rho\phi)_t + (\rho u\phi)_x + (\rho v\phi)_y = 0. \tag{6}$$

It is well-known that even when the initial data are smooth, solutions of (1)–(6) can produce complex nonsmooth wave patterns including shocks, rarefactions, and contact discontinuities. This makes it quite challenging to develop accurate and reliable numerical schemes for (1)–(6). A library of finite-volume (FV) methods for the 2-D hyperbolic systems of conservation laws have been proposed; see, e.g., the monographs [12, 15] and references therein. However, applying the single fluid FV methods to the multifluid system (1)–(6) may lead to significant pressure and velocity oscillations, which originate near the material interface and then typically spread all over the computational domain; see, e.g., [3, 13]. This occurs since in the cells where the interface is located, the fluids are artificially mixed, and the mixed cell average values often are nonphysical. Therefore, one needs to design special multifluid algorithms as it was done in, e.g., [1, 2, 4, 6, 8–10, 18–20].

In this paper, we construct a new numerical method for (1)–(6), which is, in fact, an improved version of the hybrid multifluid algorithm recently proposed in [8]. The key idea in [8] is to detect the vicinities of material interfaces and then to replace the conservative energy Eq. (4) there with a nonconservative evolution equation for the pressure p (which, unlike the total energy E, remains continuous across the contact waves at the material interfaces):

$$p_t + (up)_x + (vp)_y = -\left[(\gamma - 1)p + \gamma p_\infty\right] u_x - \left[(\gamma - 1)p + \gamma p_\infty\right] v_y. \tag{7}$$

The resulting nonconservative system (1)–(3), (5)–(7) is then solved using the path-conservative central-upwind (PCCU) scheme introduced in [5]. Away from material interfaces, the original conservative system (1)–(6) was solved in [8] using the CU scheme from [14]. We now replace that CU scheme with the recently proposed local characteristic decomposition based central-upwind (LCD-CU) scheme from [7], which contains a substantially smaller amount of numerical dissipation and typically achieves an enhanced resolution; see the numerical results for the single fluid compressible Euler equations reported in [7, §5]. In this paper, we demonstrate how the implementation of the LCD-CU scheme can enhance the resolution achieved by the hybrid multifluid algorithm.

2 Hybrid Multifluid Algorithm

We follow the hybrid multifluid algorithm from [8]. Here, we briefly describe the main steps of the algorithm and focus on the novel features of the method designed in this paper.

Step 1. Given the set of discrete data for $\boldsymbol{V} = (\rho, u, v, p, \phi)^\top$, we determine the location of the material interfaces, which are assumed to be in the immediate vicinities of the FV cells in which ϕ changes sign (for the sake of simplicity, we use uniform Cartesian meshes).

Step 2. In the vicinities of the interfaces detected in *Step 1*, we discretize the nonconservative system (1)–(3), (5)–(7) using the second-order PCCU scheme.

Step 3. Away from the detected interface areas, we discretize the conservative system (1)–(6). Unlike the method from [8], where (1)–(6) was discretized using the CU scheme from [14], we now use the LCD-CU scheme, which was recently proposed in [7] but implemented here in a slightly different way since we use an alternative piecewise linear reconstruction procedure. As in [7], we perform the reconstruction in the local characteristic variable, but in order to switch to them, we now use the primitive variables $\boldsymbol{V}$ rather than the conservative ones $(\rho, \rho u, \rho v, E, \rho\phi)^\top$. This is done as follows. First, we rewrite (1)–(6) in terms of $\boldsymbol{V}$:

$$\boldsymbol{V}_t + \mathcal{A}\boldsymbol{V}_x + \mathcal{B}\boldsymbol{V}_y = \boldsymbol{0}, \tag{8}$$

where

$$\mathcal{A} = \begin{pmatrix} u & \rho & 0 & 0 & 0 \\ 0 & u & 0 & \frac{1}{\rho} & 0 \\ 0 & 0 & u & 0 & 0 \\ 0 & \gamma(p+p_\infty) & 0 & u & 0 \\ 0 & 0 & 0 & 0 & u \end{pmatrix} \quad \text{and} \quad \mathcal{B} = \begin{pmatrix} v & 0 & \rho & 0 & 0 \\ 0 & v & 0 & 0 & 0 \\ 0 & 0 & v & \frac{1}{\rho} & 0 \\ 0 & 0 & \gamma(p+p_\infty) & v & 0 \\ 0 & 0 & 0 & 0 & v \end{pmatrix}. \tag{9}$$

We then locally linearize $\mathcal{A}$ and $\mathcal{B}$ at each x- and y-cell interfaces and obtain the linearized matrices

$$\widehat{\mathcal{A}}=\begin{pmatrix}\widehat{u} & \widehat{\rho} & 0 & 0 & 0\\ 0 & \widehat{u} & 0 & \frac{1}{\widehat{\rho}} & 0\\ 0 & 0 & u & 0 & 0\\ 0 & \widehat{\gamma}(\widehat{p}+\widehat{p}_\infty) & 0 & \widehat{u} & 0\\ 0 & 0 & 0 & 0 & \widehat{u}\end{pmatrix} \quad \text{and} \quad \widehat{\mathcal{B}}=\begin{pmatrix}v & 0 & \rho & 0 & 0\\ 0 & \widehat{v} & 0 & 0 & 0\\ 0 & 0 & \widehat{v} & \frac{1}{\widehat{\rho}} & 0\\ 0 & 0 & \widehat{\gamma}(\widehat{p}+\widehat{p}_\infty) & \widehat{v} & 0\\ 0 & 0 & 0 & 0 & \widehat{v}\end{pmatrix}, \tag{10}$$

where $\widehat{\rho}=\sqrt{\rho_L\rho_R}$, $\widehat{u}=\frac{\sqrt{\rho_L}u_L+\sqrt{\rho_R}u_R}{\sqrt{\rho_L}+\sqrt{\rho_R}}$, $\widehat{v}=\frac{\sqrt{\rho_L}v_L+\sqrt{\rho_R}v_R}{\sqrt{\rho_L}+\sqrt{\rho_R}}$, $\widehat{p}=\frac{\sqrt{\rho_L}p_L+\sqrt{\rho_R}p_R}{\sqrt{\rho_L}+\sqrt{\rho_R}}$, $\widehat{\gamma}=\frac{\sqrt{\rho_L}\gamma_L+\sqrt{\rho_R}\gamma_R}{\sqrt{\rho_L}+\sqrt{\rho_R}}$, and $\widehat{p}_\infty=\frac{\sqrt{\rho_L}(p_\infty)_L+\sqrt{\rho_R}(p_\infty)_R}{\sqrt{\rho_L}+\sqrt{\rho_R}}$, where $(\cdot)_L$ and $(\cdot)_R$ stand for the left- and right-sided point values at the given cell interface. We then use the eigenvectors of the obtained constant matrices $\widehat{\mathcal{A}}$ and $\widehat{\mathcal{B}}$ to form the (locally defined) matrices R. We then introduce the local characteristic variables $\boldsymbol{\Gamma}:=R^{-1}\boldsymbol{V}$ at every cell interface (more precisely, in two cells on the left and two cells on the right of the interface), perform the piecewise linear reconstruction in $\boldsymbol{\Gamma}$ (in our numerical experiments, we have used the Minmod2 limiter, see, e.g., [12, 15], which determines the slopes of $\boldsymbol{\Gamma}$ at each cell adjusted to the material interface), use the obtained reconstructions to evaluate the point values of $\boldsymbol{\Gamma}$ at the cell interfaces, and then compute the corresponding point values of $\boldsymbol{V}$ using $\boldsymbol{V}=R\boldsymbol{\Gamma}$.

Remark 1 Note that the nonconservative system (8)–(9) is different from (1)–(3), (5)–(7) and that it is used for the local characteristic decomposition only—not for the time evolution.

Remark 2 We perform a piecewise linear reconstruction in the local characteristic variables since when we implement the LCD-CU scheme, these variables are available and it is well-known that reconstructing local characteristic variables typically leads to smaller or no oscillations.

3 Numerical Examples

In this section, we test the proposed second-order scheme on several numerical examples and compare the obtained results with those computed by the CU and mixed-order A-WENO schemes from [8] (this scheme is based on the fifth-order WENO-Z interpolation monotonized with the help of the second-order accurate piecewise linear reconstruction). In the rest of this section, we will refer to the proposed scheme as to LCD-CU scheme. In all of the examples below, we have solved the ODE systems using the three-stage third-order strong stability preserving Runge-Kutta method (see, e.g., [11]) with CFL number 0.3.

Example 1 (*Water-Air Model Using the Stiff Equation of State*) In the first example taken from [3], we consider a gas-liquid multifluid system, in which the liquid

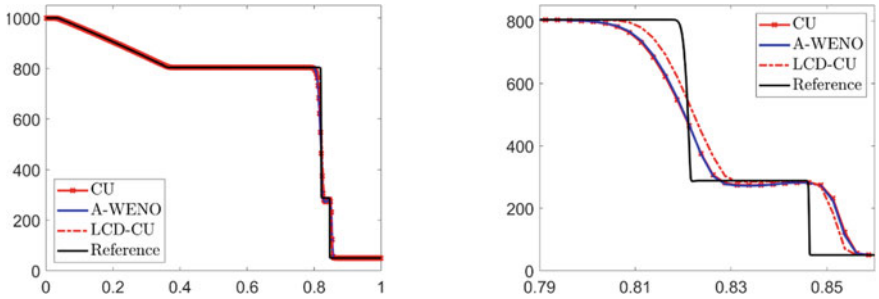

Fig. 1 Example 1: Density ρ(left) and zoom at [0.79, 0.86] (right)

component is modeled by the stiff EOS (5) with $p_\infty \gg 1$. The initial conditions correspond to a severe water-air shock tube problem and given by

$$(\rho, u, p; \gamma, p_\infty)(x, 0) = \begin{cases} (1000, 0, 10^9; 4.4, 6 \cdot 10^8), & x < 0.7, \\ (50, 0, 10^5; 1.4, 0), & x > 0.7. \end{cases}$$

We compute the numerical solution until the final time $t = 0.00025$ on a uniform mesh with 400 cells. In Fig. 1, we plot the solution computed by the CU, mixed-order A-WENO, and LCD-CU schemes together with the corresponding reference solutions computed by the LCD-CU scheme on a much finer mesh with 8000 cells. As one can see, there is no oscillations in the numerical results and the density profile obtained by the LCD-CU scheme is slightly sharper than the one computed by the second-order CU and mixed-order A-WENO schemes; see zoom at the contact and shock waves area in Fig. 1 (right).

Example 2 (*Shock Hitting Helium Bubble*) In the first 2-D example taken from [17], we consider the system (1)–(6) subject to the following initial conditions:

$$(\rho, u, v, p; \gamma, p_\infty)(x, y, 0) = \begin{cases} (4/29, 0, 0, 1; 5/3, 0), & x^2 + y^2 \le 0.0625, \\ (4/3, -0.3535, 0, 1.5; 1.4, 0), & x \ge 0.75, \\ (1, 0, 0, 1; 1.4, 0), & \text{otherwise}, \end{cases}$$

see [8, Fig. 3.6] for the sketch of the initial shock-bubble setting.

We compute the numerical results on the computational domain $[-3, 1] \times [-0.5, 0.5]$ by the second-order CU, second-order LCD-CU, and mixed-order A-WENO schemes on the uniform 2000×500 spatial mesh. In Fig. 2, we illustrate the results obtained at different time moments during the shock-bubble interaction process. Notice that the bubble changes its shape and propagates to the left, but in order to focus on the details of the bubble structure, we only zoom at $[\sigma, \sigma + 1] \times [-0.5, 0.5]$ square area containing the bubble (σ is decreasing in time from –0.75 to –1.6). We plot Schlieren images of the magnitude of the density gradient field $|\nabla\rho|$. To this end, we have used the following shading function:

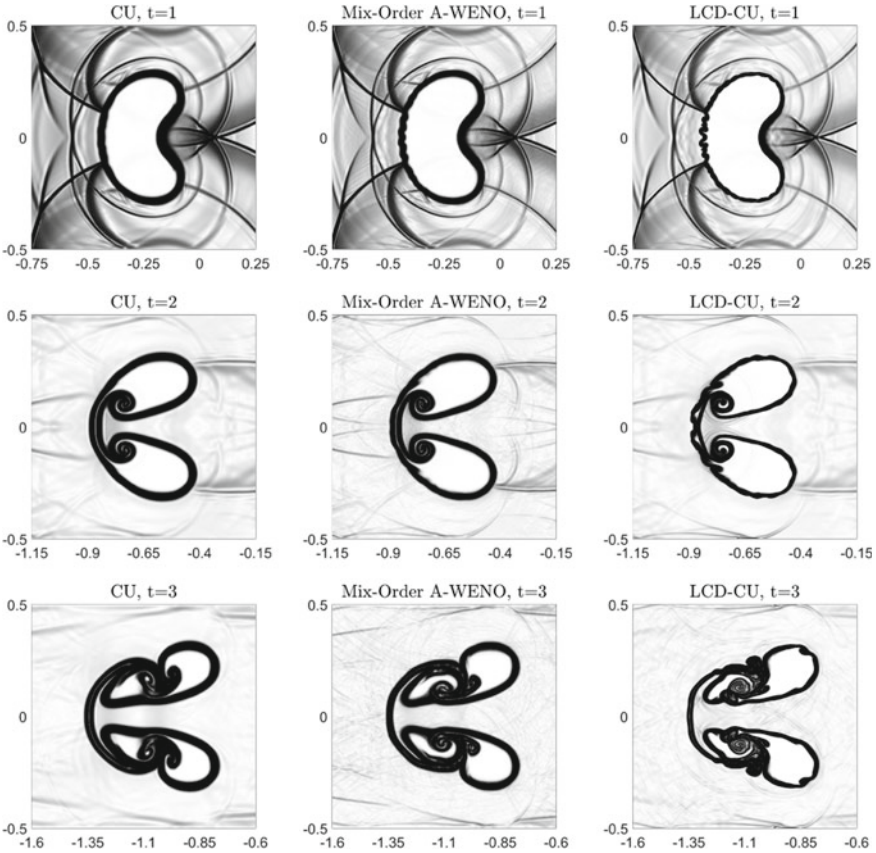

Fig. 2 Example 2: Shock-Helium bubble interaction by the CU (left column), mixed-order A-WENO (middle column), and LCD-CU (right column) schemes at $t = 1$, 2, and 3

$$\exp\left(-\frac{K|\nabla\rho|}{\max(|\nabla\rho|)}\right), \quad K = 80,$$

where the numerical density derivatives are computed using standard central differencing.

As one can see from Fig. 2, the LCD-CU scheme can capture both the material interface and small features of the solution in a sharper manner than the second-order CU and mixed-order A-WENO schemes. The differences in the results computed by the studied schemes become more pronounced at larger times.

Example 3 (*Shock Hitting R22 Bubble*) In the last example taken from [17], we consider another shock-bubble interaction problem with the following initial conditions:

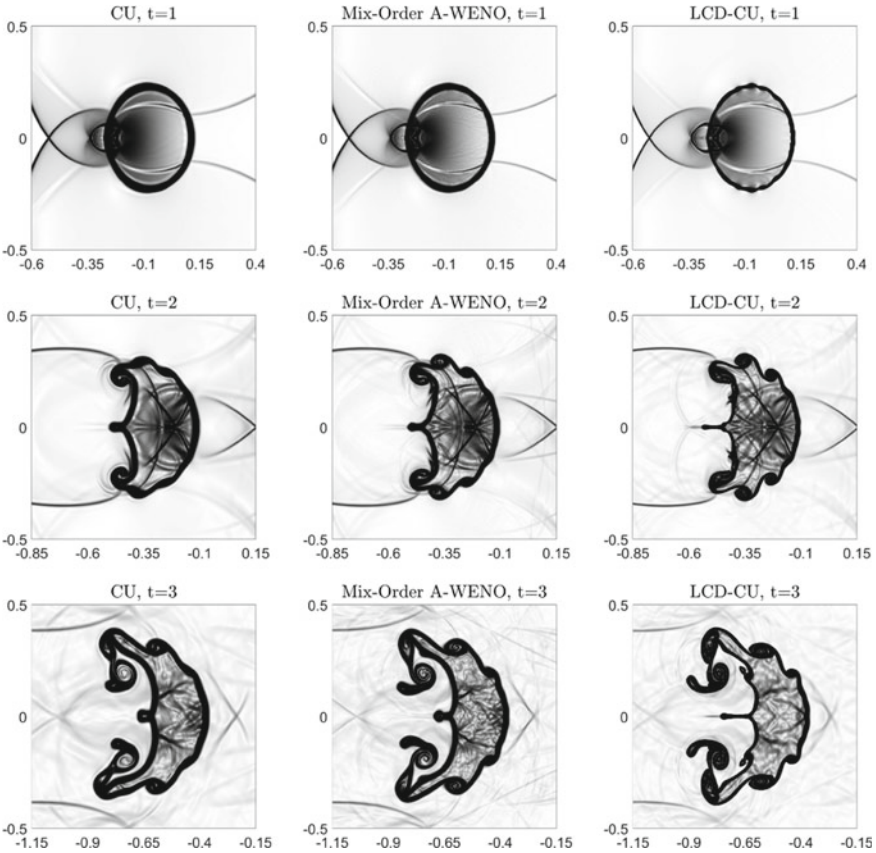

Fig. 3 Example 3: Shock-R22 bubble interaction by the CU (left column), mixed-order A-WENO (middle column), and LCD-CU (right column) schemes at $t = 1$, 2, and 3

$$(\rho, u, v, p; \gamma, p_\infty)(x, y, 0) = \begin{cases} (3.1538, 0, 0, 1; 1.249, 0), & x^2 + y^2 \le 0.0625, \\ (4/3, -0.3535, 0, 1.5; 1.4, 0), & x \ge 0.75, \\ (1, 0, 0, 1; 1.4, 0), & \text{otherwise.} \end{cases}$$

We compute the numerical results on the same computational domain and meshes as in Example 2 and plot the Schlieren images of the magnitude of the density gradient field in Fig. 3. The numerical results show that the bubble changes its shape and propagates to the left, and in order to focus on the details of the bubble structure, we only zoom at $[\sigma, \sigma + 1] \times [-0.5, 0.5]$ square area containing the bubble (σ is decreasing in time from –0.6 to –1.15). As one can see, the second-order LCD-CU scheme produces sharper numerical results than both the second-order CU and mixed-order A-WENO schemes.

Table 1 Examples 1–3: CPU times consumed by the LCD-CU and mixed-order A-WENO schemes relative to the CPU time consumed by the CU scheme

	Example 1 (%)	Example 2 (%)	Example 3 (%)
Mixed-order A-WENO	282	297	280
LCD-CU	306	328	317

Remark 3 We have measured the CPU times consumed by the studied schemes. The results obtained for Examples 1–3 are reported in Table 1, where we show the CPU time consumption of the second-order LCD-CU and mixed-order A-WENO schemes relative to the second-order CU scheme. As one can see, the times consumed by the second-order LCD-CU and mixed-order A-WENO schemes are around three times larger than times consumed by the second-order CU schemes in both 1-D and 2-D cases. It should be pointed out that even though the proposed LCD-CU scheme is more computationally expensive compared with its CU predecessor, the improvement in the achieved resolution is quite significant. If one tries to alternatively use the CU scheme on a finer mesh, the memory use may become an issue. We would also like to stress that the LCD procedure can be easily parallelized to improve the efficiency of the proposed LCD-CU scheme.

Acknowledgements The work of A. Kurganov was supported in part by NSFC grant 12171226 and by the fund of the Guangdong Provincial Key Laboratory of Computational Science and Material Design (No. 2019B030301001).

References

1. Abgrall, R., Karni, S.: Ghost-fluids for the poor: a single fluid algorithm for multifluids. In: Hyperbolic Problems: Theory, Numerics, Applications. Birkhäuser, International Series of Numerical Mathematics, vols. 140, 141, pp. 1–10 (2001). https://doi.org/10.1007/978-3-0348-8370-2_1
2. Abgrall, R., Saurel, R.A.: Discrete equations for physical and numerical compressible multiphase mixtures. J. Comput. Phys. **186**, 361–396 (2003). https://doi.org/10.1016/S0021-9991(03)00011-1
3. Abgrall, R., Karni, S.: Computations of compressible multifluids. J. Comput. Phys. **169**, 594–623 (2001). https://doi.org/10.1006/jcph.2000.6685
4. Allaire, G., Clerc, S., Kokh, S.: A five-equation model for the simulation of interfaces between compressible fluids. J. Comput. Phys. **181**, 577–616 (2002). https://doi.org/10.1006/jcph.2002.7143
5. Castro Díaz, M.J., Kurganov, A., Morales de Luna, T.: Path-conservative central-upwind schemes for nonconservative hyperbolic systems. ESAIM Math. Model. Numer. Anal. **53**, 959–985 (2019). https://doi.org/10.1051/m2an/2018077
6. Cheng, J., Zhang, F., Liu, T.G.: A quasi-conservative discontinuous Galerkin method for solving five equation model of compressible two-medium flows. J. Sci. Comput. **85**, 12–35 (2020). https://doi.org/10.1007/s10915-020-01319-5

7. Chertock, A., Chu, S., Herty, M., Kurganov, A., Lukáčová-Medvid'ová, M.: Local characteristic decomposition based central-upwind scheme. J. Comput. Phys. **473**, Paper No. 111718 (2023). https://doi.org/10.1016/j.jcp.2022.111718
8. Chertock, A., Chu, S., Kurganov, A.: Hybrid multifluid algorithms based on the path-conservative central-upwind scheme. J. Sci. Comput. **89**, Paper No. 48 (2021). https://doi.org/10.1007/s10915-021-01656-z
9. Chertock, A., Karni, S., Kurganov, A.: Interface tracking method for compressible multifluids. M2AN Math. Model. Numer. Anal. **42**, 991–1019 (2008). https://doi.org/10.1051/m2an:2008036
10. Fedkiw, R.P., Aslam, T., Merriman, B., Osher, S.: A non-oscillatory Eulerian approach to interfaces in multimaterial flows (the ghost fluid method). J. Comput. Phys. **152**, 457–492 (1999). https://doi.org/10.1006/jcph.1999.6236
11. Gottlieb, S., Shu, C.- W., Tadmor, E.: Strong stability-preserving high-order time discretization methods. SIAM Rev. **43**, 89–112 (2001). https://doi.org/10.1137/S003614450036757X
12. Hesthaven, J.S.: Numerical methods for conservation laws: from analysis to algorithms. In: Computational Science & Engineering. SIAM, PA, (2018). https://doi.org/10.1137/1.9781611975109
13. Karni, S.: Hybrid multifluid algorithms. SIAM J. Sci. Comput. **17**, 1019–1039 (1996). https://doi.org/10.1137/S106482759528003X
14. Kurganov, A., Lin, C.-T.: On the reduction of numerical dissipation in central-upwind schemes. J. Comput. Phys. **2**, 141–163 (2007). https://doi.org/10.4236/ns.2010.28114
15. LeVeque, R.J.: Finite volume methods for hyperbolic problems. In: Cambridge Texts in Applied Mathematics. Cambridge University Press, Cambridge (2002). https://doi.org/10.1017/CBO9780511791253
16. Mulder, W., Osher, S., Sethian, J.A.: Computing interface motion in compressible gas dynamics. J. Comput. Phys. **100**, 209–228 (1992). https://doi.org/10.1016/0021-9991(92)90229-R
17. Quirk, J.J., Karni, S.: On the dynamics of a shock-bubble interaction. J. Fluid Mech. **318**, 129–163 (1996). https://doi.org/10.1017/S0022112096007069
18. Saurel, R., Abgrall, R.: A simple method for compressible multifluid flows. SIAM J. Sci. Comput. **21**, 1115–1145 (1999). https://doi.org/10.1137/S1064827597323749
19. Shyue, K.M.: An efficient shock-capturing algorithm for compressible multicomponent problems. J. Comput. Phys. **142**, 208–242 (1998). https://doi.org/10.1006/jcph.1998.5930
20. Wang, C.W., Shu, C.- W.: An interface treating technique for compressible multi-medium flow with Runge-Kutta discontinuous Galerkin method. J. Comput. Phys. **229**, 8823–8843 (2010). https://doi.org/10.1016/j.jcp.2010.08.012